POLITECNICO DI TORINO
Repository ISTITUZIONALE

Shaping Closed Elastic Rings Through a Jump in Natural Curvature

Original
Shaping Closed Elastic Rings Through a Jump in Natural Curvature / Ambrosi, D., Favata, A., Paroni, R., Tomassetti, G., Turzi, S.. - In: JOURNAL OF NONLINEAR SCIENCE. - ISSN 0938-8974. - 36:5(2026), pp. 1-26. [10.1007/s00332-026-10325-0]

Availability:
This version is available at: 11583/3016176 since: 2026-09-30T15:08:07Z

Publisher:
Springer

Published
DOI:10.1007/s00332-026-10325-0

Terms of use:

This article is made available under terms and conditions as specified in the corresponding bibliographic description in the repository

Publisher copyright

(Article begins on next page)

26 November 2026

Journal of Nonlinear Science (2026) 36:108
https://doi.org/10.1007/s00332-026-10325-0

Journal of Nonlinear Science

Shaping Closed Elastic Rings Through a Jump in Natural Curvature

D. Ambrosi[1] · A. Favata[2] · R. Paroni[3] · G. Tomassetti[4,5] · S. Turzi[6]

Received: 25 May 2026 / Accepted: 8 September 2026
© The Author(s) 2026

Abstract
We investigate the shapes that a planar, inextensible closed rod can take in the presence of a piecewise inhomogeneity in its natural curvature. Since the associated mathematical problem may admit either unique or multiple solutions depending on the parameters, we reformulate the boundary value problem as a Cauchy problem with constrained initial conditions. This approach allows us to identify parameter regions corresponding to uniqueness or multiplicity of solutions; then, we exclude self-intersecting configurations. Using first integrals, geometrical arguments, perturbation analysis, and numerical simulations, we identify three distinct morphological regimes. Within a fully nonlinear framework, we determine the curves that partition the (κ, s_0) plane, where κ denotes the jump in natural curvature located at the curvilinear coordinate s_0, into regions associated with different shapes. The perturbation analysis, supported by geometrical arguments, shows good agreement with numerical results obtained from the fully nonlinear model. Our findings also apply to the equivalent case of a homogeneous rod subjected to two pointwise bending moments.

Keywords Mechanics · Morphology · Elastic rod · Euler elastica · Nonlinearity · Phase diagram

Mathematics Subject Classification Primary: 74K10 · Secondary: 74B20 · 74G60 · 34B15 · 92C10

Introduction

The Euler Elastica is the classical mathematical model to represent the mechanical behavior of a slender inextensible body (Antman 2005). The position of the material points of the rod is represented by a smooth plane curve, and the strain energy depends quadratically on the curvature. In recent years, the model has attracted renewed interest in biomechanics and mathematical biology, as it provides a natural framework to describe the mechanics of thin biological structures, possibly loaded by active stress. A

Communicated by Timothy Healey.

Extended author information available on the last page of the article

Published online: 26 September 2026

notable application concerns plant growth: growing filaments such as tendrils, roots, and shoots develop intrinsic curvature due to differential growth rates across their cross-section, and the Elastica has been used to model their coiling, buckling, and morphogenetic patterns (Goriely and Tabor 1998; Audoly and Pomeau 2010). A more recent application is the modeling of epithelial cell monolayers: The active role of molecular motors generates an asymmetry in surface tension that induces a spontaneous curvature in the epithelial sheet, making the closed-rod model particularly suitable for capturing the morphology of tubular ducts and the onset of invaginations or evaginations associated with oncogenic transformation (Krajnc et al. 2013; Haas and Goldstein 2019; Messal et al. 2019; Favata et al. June 2022).

A key mechanical observation underlies both applications: Whereas a change in natural curvature in an open rod does not generate any internal stress, and the rod simply bends to accommodate the new rest shape, the situation is fundamentally different for a closed rod. In a closed rod, geometric compatibility forces any change in natural curvature to be accompanied by a non-trivial stress distribution. This stress is the origin of a rich variety of morphological instabilities and shape transitions. Even under simple loadings, such as an uniform external pressure, the interplay between stress and geometry in closed rings leads to a complex post-buckling landscape, with multiple equilibrium branches and bifurcations that have been extensively studied (Tadjbakhsh and Odeh 1967; Healey 1988, 1990; Giomi 2013; De Pascalis et al. 2014; Napoli and Turzi 2015; Napoli and Goriely 2017, 2020). When the stress arises from a change in natural configuration, the morphological richness is comparable; a classical illustration of how intrinsic incompatibility drives shape changes in closed elastic structures is the Michell instability (Michell 1890; Goriely 2006).

In the present paper, we focus on a problem that, to the best of our knowledge, has not been yet investigated, namely the characterization of the possible shapes that a closed elastic rod with a piecewise natural curvature can take. Interestingly, this question is formally identical to assuming that the rod is subject to a couple of pointwise bending moments. Our main motivation are the numerical observations reported in Ambrosi et al. (2026). In that paper, a fully nonlinear rod model able to account for variation in thickness reveals how interface couples determine the morphology attained by a closed ring. The problem has a formal analogy with the case of variable natural curvature; however, the complexity of that model makes it difficult to obtain analytical insight into the mechanisms underlying the observed transitions.

Here we consider a simpler model, in which the rod has constant thickness and uniform bending stiffness. This simplification reduces the problem to the classical planar Euler Elastica with a piecewise natural curvature, a setting that is accessible to analytical investigation of the rich morphological landscape. In particular, we show that shapes are determined by two non-dimensional parameters and in such a parametric plane we identify the boundaries that separate different morphological states: the quasi-ring, the saddle, and the dumbbell shape.

The paper is organized as follows: In Sect. 1, we introduce the mathematical model, derive the governing equations, and provide a biological motivation of the spontaneous curvature object of the present study. In Sect. 2, we illustrate a numerical approach to investigate the existence and multiplicity of solutions, identifying regions in the parameter space where unique or multiple solutions occur. In Sect. 3, we analyze

the morphology of the solutions and interpret them in terms of trajectories in the phase plane. In Sect. 4, we derive the phase diagram and characterize the boundaries separating the different morphological regimes. In Sect. 5, we develop a linearized analysis and compare its predictions with the fully nonlinear results. Finally, in Sect. 6 we summarize the main findings and discuss their implications for the applications introduced above.

1 The Mechanical Model

We consider a closed inextensible elastic rod; the position of its material points is described by a curve spanned by the curvilinear coordinate $0 \leq s \leq 2\ell$. We assume that the mechanical properties of the rod (stiffness, natural curvature) are piecewise constant and, in particular, they take a constant value in $0 \leq s \leq s_0, 2\ell - s_0 \leq s \leq 2\ell$ and another one in $s_0 \leq s \leq 2\ell - s_0$. Under such an assumption, we can exploit the symmetry of the problem and we restrict our analysis to half a rod.

1.1 Kinematics

For mathematical convenience, we write the position of the points of the rod as two curves, with suitable interface conditions. In particular,

$$\mathbf{r}_1(s_1) : [0, s_0] \to \mathbb{R}^2, \qquad 0 \leq s_1 \leq s_0, \tag{1}$$

$$\mathbf{r}_2(s_2) : [s_0, \ell] \to \mathbb{R}^2, \qquad s_0 \leq s_2 \leq \ell. \tag{2}$$

With an abuse of notation, we shall denote both s_1 and s_2 with the same symbol s from now on, without the possibility of confusion. The position of the material points of the rod is described by arclength parametrization with the vector field:

$$\mathbf{r}_1(s) = (x_1(s), y_1(s)) \qquad \mathbf{r}_2(s) = (x_2(s), y_2(s)). \tag{3}$$

The following boundary conditions are dictated by the symmetry of the problem:

$$\mathbf{r}_1(0) = (0, 0), \qquad x_2(\ell) = 0. \tag{4}$$

Moreover, the continuity of the position vector requires that:

$$\mathbf{r}_1(s_0) = \mathbf{r}_2(s_0). \tag{5}$$

The remaining conditions concern the tangent vector $\mathbf{t}_i(\theta_i) = (\cos(\theta_i), \sin(\theta_i))$, which is uniquely defined in every point of each planar curve, where $\theta_i(s_i)$ is the angle between the tangent vector and the x-axis, anticlockwise defined. Normal unit vectors are then $\mathbf{n}_i(\theta_i) = (\sin(\theta_i), -\cos(\theta_i))$ so that $(\mathbf{t}_i(\theta_i))' = -\mathbf{n}_i(\theta_i)\theta_i'$, where the prime denotes the derivative in s (see Fig. 1 for a sketch with the relevant geometric quantities).

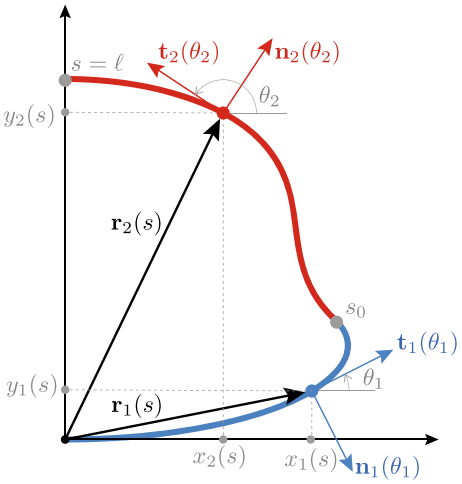

Fig. 1 Schematic illustration of the rod geometry and of the notation and conventions used in the analysis. The curve is parametrized by the arclength s, with the natural-curvature discontinuity located at $s = s_0$. The vectors $\mathbf{r}_i(s)$, $\mathbf{t}_i(\theta_i)$, and $\mathbf{n}_i(\theta_i)$ denote, respectively, the position, unit tangent, and unit normal along the two branches of the rod, while θ_i gives the tangent angle measured from the reference axis

Concerning the angles θ_i, we require

$$\theta_1(0) = 0, \qquad \theta_2(\ell) = \pi. \tag{6}$$

In addition, continuity of the tangent vector yields the condition

$$\theta_1(s_0) = \theta_2(s_0). \tag{7}$$

1.2 Equilibrium equations

An inextensible rod stores elastic energy only because of bending:

$$w = \int_0^{s_0} \frac{\mu_1}{2}(\theta_1')^2 ds + \int_{s_0}^{\ell} \frac{\mu_2}{2}(\theta_2' + \kappa)^2 ds, \tag{8}$$

where μ_1, μ_2 are bending moduli and κ is the natural curvature of the second rod, the first one having null natural curvature. These assumptions do not restrain the generality of the analysis, as will be discussed below. We append the inextensibility constraint to the energy, and we get the functional

$$\begin{aligned} W(\theta_i, \mathbf{r}_i, \mathbf{N}_i) = {} & \frac{\mu_1}{2}\int_0^{s_0} (\theta_1')^2\, ds + \frac{\mu_2}{2}\int_{s_0}^{\ell} (\theta_2' + \kappa)^2\, ds \\ & - \int_0^{s_0} \mathbf{N}_1 \cdot \big(\mathbf{r}_1' - \mathbf{t}_1(\theta_1)\big)\, ds - \int_{s_0}^{\ell} \mathbf{N}_2 \cdot \big(\mathbf{r}_2' - \mathbf{t}_2(\theta_2)\big)\, ds, \end{aligned} \tag{9}$$

where $\mathbf{N}_i(s_i) = (N_i^x(s_i), N_i^y(s_i))$ is the (unknown) reaction force in the i-th rod. After first-order variation and integration by parts, we get

$$\begin{aligned}\delta W = &- \int_0^{s_0} \left(\mu_1\theta_1'' + \mathbf{N}_1 \cdot \mathbf{n}_1(\theta_1)\right) \delta\theta_1 \, ds + \mu_1 \left[\theta_1' \delta\theta_1\right]_0^{s_0} \\ &- \int_{s_0}^{\ell} \left(\mu_2(\theta_2' + \kappa)' + \mathbf{N}_2 \cdot \mathbf{n}_2(\theta_2)\right) \delta\theta_2 \, ds + \mu_2 \left[(\theta_2' + \kappa)\delta\theta_2\right]_{s_0}^{\ell} \\ &+ \int_0^{s_0} \mathbf{N}_1' \cdot \delta\mathbf{r}_1 \, ds + \int_{s_0}^{\ell} \mathbf{N}_2' \cdot \delta\mathbf{r}_2 \, ds - \left[\mathbf{N}_1 \cdot \delta\mathbf{r}_1\right]_0^{s_0} - \left[\mathbf{N}_2 \cdot \delta\mathbf{r}_2\right]_{s_o}^{\ell} \\ &- \int_0^{s_0} \left(\mathbf{r}_1' - \mathbf{t}_1(\theta_1)\right) \cdot \delta\mathbf{N}_1 \, ds - \int_{s_0}^{\ell} \left(\mathbf{r}_2' - \mathbf{t}_2(\theta_2)\right) \cdot \delta\mathbf{N}_2 \, ds.\end{aligned} \tag{10}$$

Requiring that $\delta W = 0$ for every admissible variation yields the following Euler–Lagrange equations

$$\mu_1\theta_1'' = -\mathbf{N}_1 \cdot \mathbf{n}_1 \qquad \mu_2\theta_2'' = -\mathbf{N}_2 \cdot \mathbf{n}_2, \tag{11a}$$
$$\mathbf{N}_1' = 0, \qquad \mathbf{N}_2' = 0, \tag{11b}$$
$$\mathbf{r}_1' = \mathbf{t}_1(\theta_1), \qquad \mathbf{r}_2' = \mathbf{t}_2(\theta_2), \tag{11c}$$

supplemented by the boundary and interface conditions

$$\theta_1(0) = 0, \qquad \theta_2(\ell) = \pi, \tag{12a}$$
$$\theta_1(s_0) = \theta_2(s_0), \qquad \mu_1\theta_1'(s_0) = \mu_2(\theta_2'(s_0) + \kappa), \tag{12b}$$
$$\mathbf{N}_1(s_0) = \mathbf{N}_2(s_0), \qquad \mathbf{r}_1(s_0) = \mathbf{r}_2(s_0), \tag{12c}$$
$$\mathbf{r}_1(0) = (0, 0), \qquad x_2(\ell) = 0, \qquad \mathbf{N}(\ell) = (N, 0), \tag{12d}$$

where the last condition follows from (4) and

$$\mathbf{N}(\ell) \cdot \delta\mathbf{r}_2(\ell) = \mathbf{N}(\ell) \cdot (0, \delta y_2(\ell)) = 0 \qquad \forall \delta y_2(\ell). \tag{13}$$

Equations (11b), (12c), and (12d) tell us that the reaction vector has only a horizontal non-null constant component, which we identify with N. The system of equations eventually rewrites:

$$\mu_1\theta_1'' = -N\sin(\theta_1), \qquad \mu_2\theta_2'' = -N\sin(\theta_2) \tag{14a}$$
$$\mathbf{r}_1' = (\cos(\theta_1), \sin(\theta_1)), \qquad \mathbf{r}_2' = (\cos(\theta_2), \sin(\theta_2)), \tag{14b}$$

with boundary and interface conditions

$$\theta_1(0) = 0, \qquad \theta_2(\ell) = \pi, \tag{15a}$$
$$\theta_1(s_0) = \theta_2(s_0), \qquad \mu_1\theta_1'(s_0) = \mu_2(\theta_2'(s_0) + \kappa), \tag{15b}$$
$$\mathbf{r}_1(0) = (0, 0), \qquad \mathbf{r}_1(s_0) = \mathbf{r}_2(s_0), \qquad x_2(\ell) = 0. \tag{15c}$$

1.3 Equations in non-dimensional form

To simplify the analysis from now on, we take $\mu_1 = \mu_2 = \mu$. We discuss the minor relevance of this assumption in a remark below.

We rewrite the equations in a dimensionless form introducing the reference length ℓ and the reference bending modulus μ. We define the non-dimensional quantities

$$\tilde{s} = s/\ell, \quad \tilde{\mathbf{r}}_1 = \mathbf{r}_1/\ell, \quad \tilde{\mathbf{r}}_2 = \mathbf{r}_2/\ell, \quad \tilde{N} = N\ell^2/\mu, \quad \tilde{\kappa} = \kappa\ell, \quad \tilde{s}_0 = s_0/\ell, \tag{16}$$

and, dropping the tilde symbols from now on, equations (14) rewrite

$$\theta_1'' = -N\sin(\theta_1), \qquad \theta_2'' = -N\sin(\theta_2), \tag{17}$$

$$\mathbf{r}_1' = (\cos(\theta_1), \sin(\theta_1)), \qquad \mathbf{r}_2' = (\cos(\theta_2), \sin(\theta_2)), \tag{18}$$

with boundary and interface conditions

$$\mathbf{r}_1(0) = (0,0), \qquad x_2(1) = 0, \qquad \mathbf{r}_1(s_0) = \mathbf{r}_2(s_0), \tag{19}$$

$$\theta_1(0) = 0, \qquad \theta_2(1) = \pi, \qquad \theta_1(s_0) = \theta_2(s_0), \qquad \theta_1'(s_0) = \theta_2'(s_0) + \kappa. \tag{20}$$

Equations (19–20) provide the nine boundary conditions for the (equivalent) first-order differential system in the unknowns $(\mathbf{r}_1, \mathbf{r}_2, \theta_1, \theta_1', \theta_2, \theta_2', N)$. In the rest of the paper, to simplify the notation, we shall use the symbol

$$\theta_0 := \theta_1(s_0) = \theta_2(s_0) \tag{21}$$

to denote the common value of $\theta_1(s_0)$ and $\theta_2(s_0)$.

Remark 1 Without loss of generality, we can restrict our analysis to the case $\kappa \geq 0$. To see this, suppose $\bar{\theta}_1(s), \bar{\theta}_2(s)$ is a solution of equations (17)–(18) corresponding to the parameters $(-\bar{\kappa}, \bar{s}_0)$ with $\bar{\kappa} > 0$. Define

$$\tilde{\theta}_1(s) = \pi - \bar{\theta}_2(1-s), \qquad \tilde{\theta}_2(s) = \pi - \bar{\theta}_1(1-s).$$

Then $(\tilde{\theta}_1, \tilde{\theta}_2)$ is a solution corresponding to parameters $(+\bar{\kappa},\ 1-\bar{s}_0)$. Geometrically, this transformation is a reflection of the rod about the axis $\theta = \pi/2$, combined with swapping the two portions. Hence, every solution with $\kappa < 0$ and junction at s_0 is the mirror image of a solution with $\kappa > 0$ and junction at $1 - s_0$, and the phase diagram in the (κ, s_0) plane with $\kappa \geq 0$ is complete.

1.4 On the physical origin of the natural curvature

A possible physical mechanism that generates the effective natural curvature κ is the presence of distinct surface tensions on the upper and lower faces of the rod. This is particularly relevant in the context of epithelial sheets, where the activity of actin-myosin

molecular motors at the apical and basal cortex generates an asymmetry between the apical and basal surface tensions (Krajnc et al. 2013; Khalilgharibi et al. 2020). This mechanical asymmetry induces a spontaneous bending tendency in the epithelial sheet, which is the mechanobiological origin of the natural curvature parameter κ in our model. Below we present a heuristic derivation of the surface tension-induce natural curvature.

Consider a rod with rectangular cross section of length L, width w, and thickness h, and assume that

$$\varepsilon = \frac{h}{L} \ll 1. \tag{22}$$

The bending energy of the rod is

$$\mathcal{E}_{\text{bulk}} = \frac{\varepsilon^3 w L^3 E}{12} \int_0^L \frac{1}{2}\theta'^2(s)\, ds, \tag{23}$$

where E is the Young modulus and θ' is the curvature of the centerline, Antman (2005). In addition, the surface energy contribution from the upper (+) and lower (−) faces, associated with the apical and basal surface tensions $\gamma_\pm$, is:

$$\mathcal{E}_{\text{surf}} = w \left(\int_0^L \gamma_+(s)\, ds_+ + \int_0^L \gamma_-(s)\, ds_- \right). \tag{24}$$

Since the rod is inextensible, the arclength elements on the upper and lower faces relate to the centerline curvature by

$$ds_\pm = \left(1 \pm \frac{\varepsilon L}{2}\,\theta'\right) ds. \tag{25}$$

Substituting into $\mathcal{E}_{\text{surf}}$ yields

$$\mathcal{E}_{\text{surf}} = w \int_0^L \left[(\gamma_+ + \gamma_-) + \frac{\varepsilon L}{2}(\gamma_+ - \gamma_-)\,\theta' \right] ds. \tag{26}$$

The first term is constant for an inextensible rod and plays no role in the equilibrium problem. The total energy therefore reduces to

$$\mathcal{E} = \frac{\varepsilon^3 w L^3 E}{12} \int_0^L \left(\frac{1}{2}\theta'^2 + \kappa\,\theta' \right) ds + \text{const}, \tag{27}$$

where the effective natural curvature is

$$\kappa = \frac{6(\gamma_+ - \gamma_-)}{E h^2}. \tag{28}$$

Completing the square in (27) and introducing the bending stiffness

$$\mu = EI, \qquad I = w\frac{(\varepsilon L)^3}{12}, \tag{29}$$

the total energy takes the standard form

$$\mathcal{E} = \frac{\mu}{2}\int_0^L (\theta' + \kappa)^2\, ds + \text{const}, \tag{30}$$

which is the classical bending energy of a rod with (possibly non-constant) natural curvature κ. Thus, an imbalance between apical and basal surface tensions ($\gamma_+ \neq \gamma_-$), driven by differential actin activity, is equivalent at leading order to imposing a nonzero natural curvature on the rod (Krajnc et al. 2013). In the piecewise setting of the present paper, a jump in surface tension across a portion of the ring, as occurs when a subset of epithelial cells undergoes oncogenic transformation, rewrites as a jump in the natural curvature κ, which is the central parameter of our model.

2 Existence and Multiplicity of Solutions: A Numerical Investigation

Equations (17–18) supplemented by the boundary and interface conditions (19–20) define a second-order boundary value problem that, in general, may have unique or multiple solutions (Lions et al. 2012). To investigate the multiplicity of solutions depending on the non-dimensional parameters (κ, s_0), the boundary value problem is reformulated as an initial-value problem, for which existence and uniqueness are guaranteed by the Cauchy–Lipschitz theorem. In our setting, this amounts to fix N and prescribe the initial condition $\theta_1'(0) =: M$. For given (κ, s_0), the corresponding Cauchy problem has unique solution that, in general, does not satisfy the boundary conditions at the endpoint of the original boundary value problem. We then tune the parameters (M, N) and record for which values the endpoint conditions at $s = 1$, namely $\theta_2(1) = \pi$ and $x_1(1) = 0$, are satisfied. This methodology will provide us an information about the multiplicity of the solutions.

For $s_0 \in [0, 1]$ and $\kappa \in (0, +\infty)$ fixed, we define $\theta_1(\cdot; M, N) : [0, s_0] \to \mathbb{R}$ the unique solution of the following initial-value problem on $(0, s_0)$:

$$\begin{cases} \theta_1'' + N \sin\theta_1 = 0, \\ \theta_1(0) = 0, \\ \theta_1'(0) = M. \end{cases}$$

Then, for

$$\theta_0 := \theta_1(s_0; M, N), \qquad \kappa_0 := \frac{\partial}{\partial s}\bigg|_{s=s_0} \theta_1(s; M, N),$$

we let $\theta_2(\cdot; M, N) : [s_0, 1] \to \mathbb{R}$ be the unique solution of the following initial-value problem on $(s_0, 1)$:

$$\begin{cases} \theta_2'' + N \sin\theta_2 = 0, \\ \theta_2(s_0) = \theta_0, \\ \theta_2'(s_0) = \kappa_0 - \kappa. \end{cases}$$

The shape of the rod is described by:

$$\begin{aligned} x_1(s; M, N) &= \int_0^s \cos\theta_1(s; M, N) ds, \\ y_1(s; M, N) &= \int_0^s \sin\theta_1(s; M, N) ds, \end{aligned} \qquad s \in [0, s_0], \tag{31}$$

and

$$\begin{aligned} x_2(s; M, N) &= x_1(s_0; M, N) + \int_0^s \cos\theta_2(s; M, N) ds, \\ y_2(s; M, N) &= y_1(s_0; M, N) + \int_0^s \sin\theta_2(s; M, N) ds, \end{aligned} \qquad s \in [s_0, 1]. \tag{32}$$

We then define the maps $F : \mathbb{R}^2 \to \mathbb{R}^2$ and $G : \mathbb{R}^2 \to \mathbb{R}^2$ by

$$\begin{cases} F(M, N) := \theta_2(1; M, N) - \pi, \\ G(M, N) := x_2(1; M, N). \end{cases} \tag{33}$$

For each pair (s_0, κ), finding an equilibrium shape corresponds to solving for $(M, N) \in \mathbb{R}^2$ the system of algebraic equations

$$\begin{cases} F(M, N) = 0, \\ G(M, N) = 0. \end{cases} \tag{34}$$

The first equation enforces the conditions that the final orientation of the rod is π, while the second equation corresponds to require that the $x_1(s = 1) = 0$.

To compute the solutions of equations (34) numerically, we consider a structured grid of initial guesses in the (M, N)-plane. In MATLAB, this grid can be generated using the command `meshgrid`, and the resulting points are then used as initial guesses for the `fsolve` routine.

Geometrically, each of the two equations of (34) defines a curve on the plane. The solution set is thus the intersection of these two curves. An illustrative example is in Fig. 2, where three solutions are shown, marked by the letters **A**, **B**, and **C**. Self-intersecting solutions, which cross the axis $y = 0$, are regarded as non-physical and will therefore be discarded throughout the remainder of this article. In the language of differential geometry, we are only interested in *simple* solutions (Manfredo 1976). For instance, among the solutions **A**, **B**, and **C**, only two have physical significance, since solution **C** crosses the axis $y = 0$.

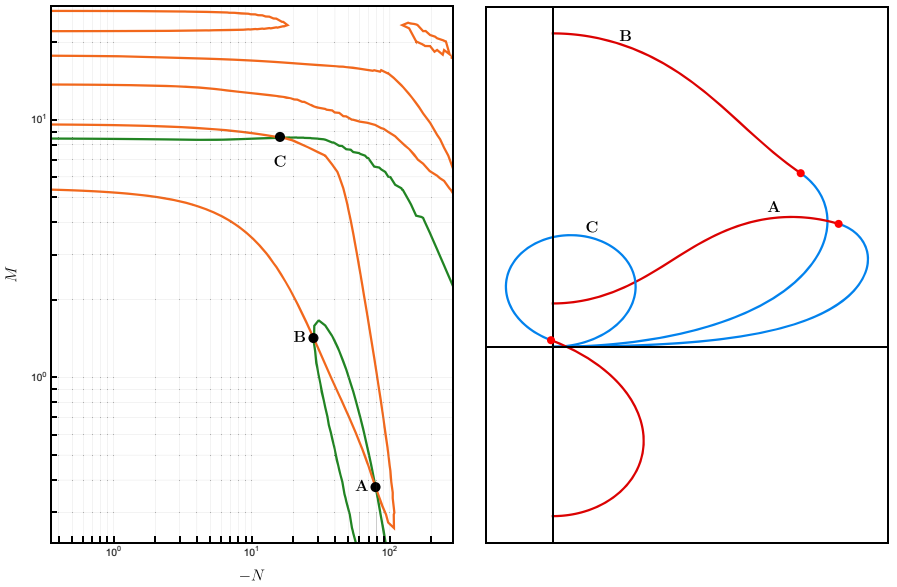

Fig. 2 Left: zero-level curves of $F(M, N)$ and $G(M, N)$ for $(s_0, \kappa) = (0.57, 12.4)$. The intersections of these curves correspond to the equilibrium configurations **A**, **B**, and **C**. Right: equilibrium shapes. The **C** solution crosses the axis of symmetry $x = 0$ and is discarded

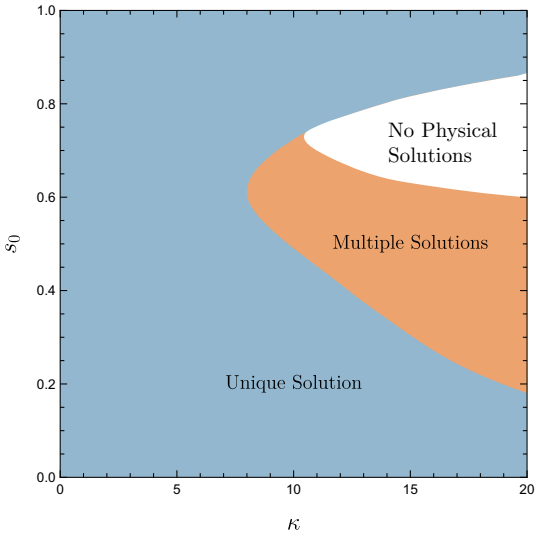

Fig. 3 Partition of the (s_0, κ) plane in regions according to the multiplicity of solutions. Blue: one physical (i.e., simple) solution. Orange: multiple physical solutions. White: no physical solution

By sweeping the (s_0, κ) plane with a sufficiently dense set of point, we are able to identify distinct regions according to the number of physical solutions. The regions in the (s_0, κ)-plane where a unique solution, multiple solutions, or no physical solution exist, are shown in Fig. 3.

Remark 2 The parameters (M, N) are numerically explored in a rectangle of $\mathbb{R}^2$. While we cannot provide a rigorous argument for the size of our exploration region, we know that solutions outside this domain are not expected to yield physically relevant configurations.

From a physical standpoint, $M = \theta_1'(0)$ represents the reactive bending moment in $s = 0$, while N is the tension. Large values of M correspond to configurations with very high curvature near the clamped end, which typically lead to strongly bent or oscillatory shapes, often involving self-intersections or sharp turns that are not admissible in our physical model. In the same vein, according to equation (14a) N is a force times a square length, the length representing the typical spatial distance of variation of the solution. Therefore, large values of N correspond to rapidly oscillating solutions of the Elastica equation, again resulting in configurations that lack physical relevance.

3 Morphology of the Solutions and Phase Portrait

When multiple physical solutions are present, it is natural to select those with minimal energy. We emphasize that this is merely a selection criterion: throughout the paper we display, at each point of the parameter space, the lowest-energy configuration among the physical equilibria, without implying that the remaining equilibria are necessarily unstable.

However, even if we restrict ourselves to minimum-energy solutions, a variety of morphologies can still be observed as illustrated in Fig. 4.

Inspection of Fig. 4 reveals three possible shapes of the physical solutions: *quasi-ring* (**R**), *saddle* (**S**), and *dumbbell* (**D**).

A quantitative characterization of these shapes can be supported exploiting the formal analogy between equations (17) and the pendulum. Notice that equations (17) admit the first integrals

$$\frac{1}{2}(\theta_i')^2 - N\cos(\theta_i) = C_i, \qquad i = 1, 2, \tag{35}$$

where C_1 and C_2 are constants to be determined. A representation of the solution in the phase plane $(\theta(s), \theta'(s))$ defines a discontinuous trajectory (see Fig. 5).

Each simple curve is composed by two branches, which, for the sake of clarity, we denote by γ_1 and γ_2. Notice that the constant C_1 is related to the constant M of the previous section by the relation $M^2 = 2(C_1 + N)$. Consistently with equations (20), the curves satisfy the following endpoint conditions:

$$\left(\theta_1'(0)\right)^2 = 2(C_1 + N) \tag{36}$$

$$\theta_1'(s_0) - \theta_2'(s_0) = \kappa \tag{37}$$

$$\left(\theta_2'(1)\right)^2 = 2(C_2 - N). \tag{38}$$

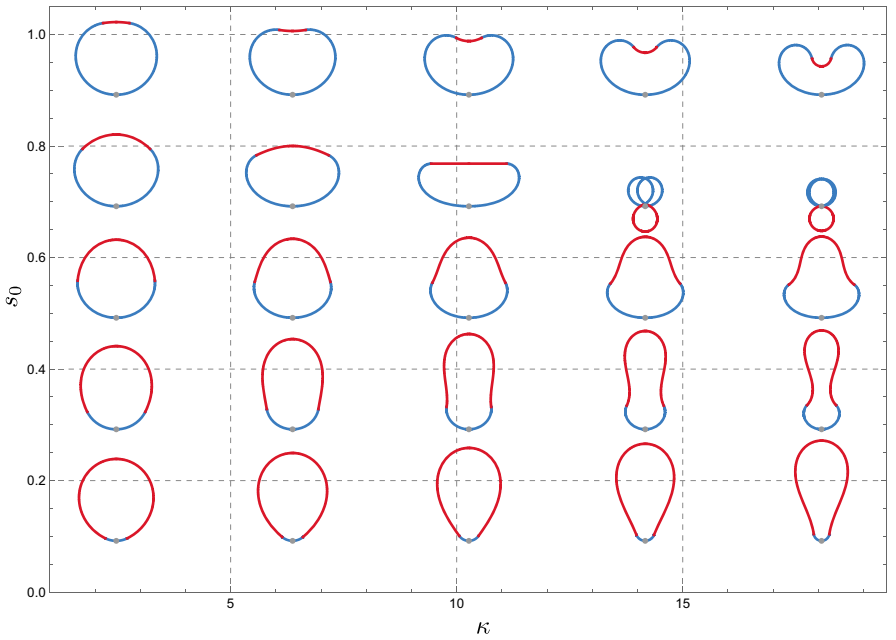

Fig. 4 Morphological diagram obtained numerically spanning the (k, s_0) parametric plane: among possible multiple solutions we discard self–intersecting ones and choose the one with minimum energy

The three observed morphologies can be quantitatively described as follows, depending on the number of zeros of the curvature θ' along the rod.

Quasi-ring (positive curvature, Figure 5R) If θ_1' in θ_0 is larger than κ, according to (37) the curve γ_2 belongs to the same half plane of γ_1 ($\theta' > 0$) and eventually reaches the value $\theta_2(1) = \pi$. In this case, the curvature of the rod does not change sign. Notice that γ_1 must be a portion of an open curve in the phase space ($C_1 + N > 0$) so that the value $\theta_1 = 0$ can be the left endpoint of the curve. The curve γ_2 can either be open or closed.

If the jump of the curvature in θ_0 is larger than κ, then $\theta_2'(\theta_0)$ is negative and two possible scenarios occur.

Saddle (the curvature changes sign once, Figure 5 S) If $\theta_0 > \pi$, i.e. γ_1 goes beyond $\theta_1 = \pi$, where the curvature takes its maximum value. The curve runs clockwise until the value $\theta_2 = \pi$ is reached, the endpoint of the rod. In the physical space, this space corresponds to a positive curvature that changes sign in s_0. Also in this case, the curve γ_2 can either be open or closed. We remark that the morphology of the saddle depends only on the number of sign changes. In particular, we do not distinguish between positive and negative values of $\theta_2'(\theta_0)$, since its sign does not affect the shape of the saddle.

Dumbbell (the curvature changes sign twice, Figure 5D) If $\theta_0 < \pi$, the large jump in curvature again takes to a curve γ_2 with negative curvature. As curves are always run

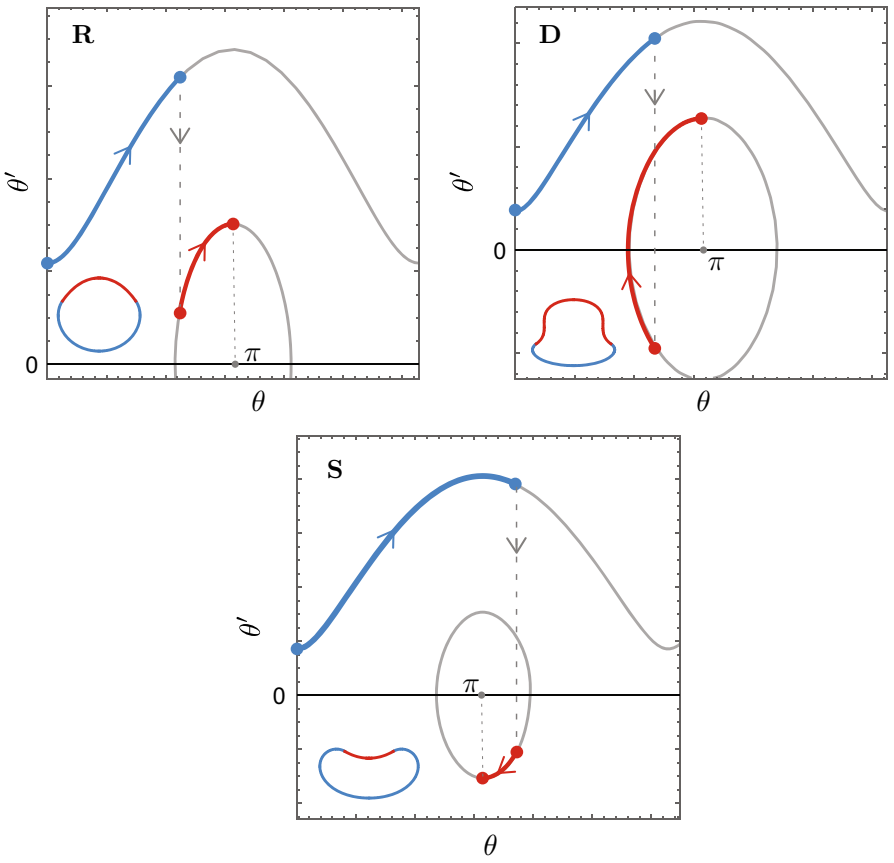

Fig. 5 Phase-space trajectories corresponding to the three prototypical configurations **R**, **D**, and **S**

in clockwise sense, γ_2 crosses the $\theta' = 0$ axis and changes again (smoothly) the sign of the curvature again. The curve γ_2 must belong to a closed orbit ($C_2 + N < 0$).

Remark 3 It is now possible to better understand why no generality is lost in our analysis by taking the same bending stiffness in (15b). If $\kappa = 0$, the curvature jump induced by two different μ_1 and μ_2 (as given in the boundary condition (12b)) can only preserve the sign of θ', so that only quasi-ring shapes are produced. A richer morphology arises from κ. The extension of the results to the case of jumps in both bending stiffness and natural curvature is therefore straightforward.

4 Analytical Derivation of the Phase Diagram

We observe in Fig. 4 that the three prototypical shapes illustrated in the previous section do not appear scattered in the (s_0, κ) plane: three regions can be identified, each one corresponding to a different morphology. We refer to these regions as "phases", that

are likely separated by curves that are therefore the "phase boundaries". In this section, we identify the conditions that define the phase boundary curves.

Remark 4 The term "phase" in this paper occurs with two distinct meanings: the phase portrait is the curve solution in the (θ, θ') plane (see Fig. 5), while the phase diagram defines the boundary between different morphological regions in the (k, s_0) plane (see Fig. 4). The former terminology is inherited from dynamical systems, the latter from thermodynamics.

Equation (35) can be rewritten as:

$$\frac{d\theta_i}{ds} = \pm\sqrt{2(C_i + N\cos\theta_i)}, \qquad i = 1, 2 \tag{39}$$

where the sign is positive or negative according to whether θ_i is increasing or decreasing. The sign is not unique: it is fixed by the type of solution we are looking for (see Fig. 5). We can solve this equation in general by separating the variables

$$ds = \pm\frac{d\theta_i}{\sqrt{2(C_i + N\cos\theta_i)}}, \qquad i = 1, 2. \tag{40}$$

We choose positive sign when $d\theta$ and ds have the same sign, negative otherwise. Likewise, the differential of the x coordinate is given by $dx_i = \cos(\theta_i)ds$, whence:

$$dx_i = \pm\frac{\cos(\theta_i)d\theta_i}{\sqrt{2(C_i + N\cos\theta_i)}}, \qquad i = 1, 2. \tag{41}$$

Moreover, the condition $(20)_4$ on the derivative jump rewrites as

$$\pm\sqrt{2(C_1 + N\cos\theta_0)} = \pm\sqrt{2(C_2 + N\cos\theta_0)} + \kappa \tag{42}$$

where we recall that $\theta_0 = \theta(s_0)$, and the signs depend on whether θ_1 and θ_2 are increasing or decreasing functions at $s = s_0$.

We will use these equations to identify the boundaries between regions configurationally different in the (κ, s_0) plane. In particular, we want to identify the curves separating the solutions: (a) quasi-ring, (b) dumbbell, and (c) saddle illustrated in Sect. 2 (Fig. 6).

For given (κ, s_0), we are now able to characterize the equilibrium solution in terms of four constants C_1, C_2, θ_0, N. For example, to identify the type (a) solution, where θ_1 and θ_2 are always increasing functions of s, we obtain C_1, C_2, θ_0, N for given values of the parameters s_0 and κ from the integral-algebraic equations:

$$s_0 = \int_0^{\theta_0} \frac{d\theta_1}{\sqrt{2(C_1 + N\cos\theta_1)}}, \tag{43a}$$

$$1 - s_0 = \int_{\theta_0}^{\pi} \frac{d\theta_2}{\sqrt{2(C_2 + N\cos\theta_2)}}, \tag{43b}$$

$$\sqrt{2(C_1 + N\cos\theta_0)} = \sqrt{2(C_2 + N\cos\theta_0)} + \kappa, \tag{43c}$$

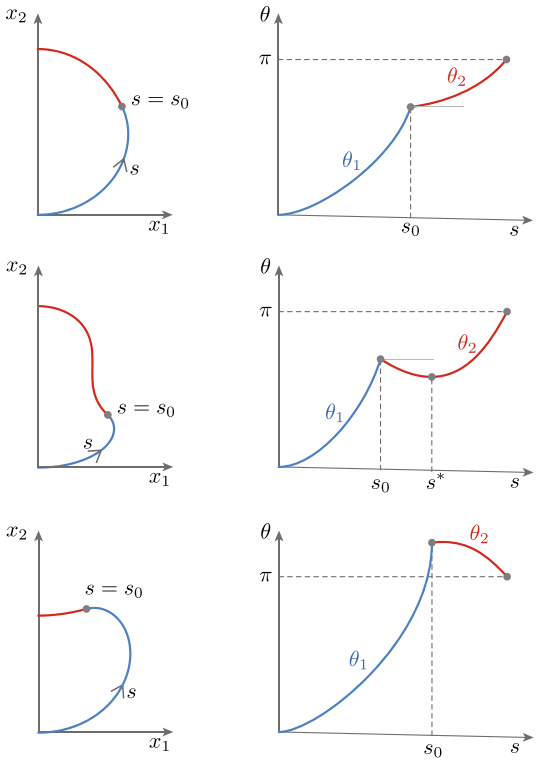

Fig. 6 Morphology of solutions: quasi-ring shape, dumbbell shape, and saddle shape

$$\int_0^{\theta_0} \frac{\cos(\theta_1)d\theta_1}{\sqrt{2(C_1 + N\cos\theta_1)}} + \int_{\theta_0}^{\pi} \frac{\cos(\theta_2)d\theta_2}{\sqrt{2(C_2 + N\cos\theta_2)}} = 0. \tag{43d}$$

4.1 Transition to a saddle-like solution

Solutions (a) and (b) can be distinguished from (c) because in the saddle-type solution (c), $\theta_0 > \pi$. The limiting condition separating the two regions is thus $\theta_0 = \pi$. In this case, the solution in the interval $[s_0, 1]$ is simply a flat segment with $\theta_2(s) = \pi$, $s \in [s_0, 1]$. From (35), we immediately obtain $C_2 = N$, while C_1, N, and κ are given by the equations

$$s_0 = \int_0^{\pi} \frac{d\theta_1}{\sqrt{2(C_1 + N\cos\theta_1)}}, \tag{44a}$$

$$1 - s_0 = \int_0^{\pi} \frac{\cos\theta_1}{\sqrt{2(C_1 + N\cos\theta_1)}} d\theta_1, \tag{44b}$$

$$\kappa = \sqrt{2(C_1 - N)}, \tag{44c}$$

where equation (44b) follows from $x_1(s_0) = 1 - s_0$.

4.2 Transition to a dumbbell-like solution

For the dumbbell-like solution, there is a point s^* where $\theta_2'(s^*) = 0$, which is a minimum point of θ_2. The limiting case, which defines the boundary of this region, occurs when $s_0 = s^*$, i.e., the minimum point coincides with the separation point between the two portions of the rod.

We therefore impose $\theta_2'(s_0) = 0$ in the equations. Substituting this condition in (35) for $i = 2$, evaluated at $s = s_0$, yields

$$C_2 = -N \cos\theta_0. \tag{45}$$

Furthermore, from the jump condition $(20)_4$ we obtain $\theta_1'(s_0) = \kappa$, which implies, by (35) with $i = 1$, that

$$C_1 = \frac{\kappa^2}{2} - N \cos\theta_0. \tag{46}$$

The three equations that define the values of θ_0, N, κ at the transition are therefore

$$s_0 = \int_0^{\theta_0} \frac{1}{\sqrt{\kappa^2 + 2N\,(\cos\theta_1 - \cos\theta_0)}}\, d\theta_1, \tag{47a}$$

$$1 - s_0 = \int_{\theta_0}^{\pi} \frac{1}{\sqrt{2N\,(\cos\theta_2 - \cos\theta_0)}}\, d\theta_2, \tag{47b}$$

$$\int_0^{\theta_0} \frac{\cos\theta_1}{\sqrt{\kappa^2 + 2N\,(\cos\theta_1 - \cos\theta_0)}}\, d\theta_1 + \int_{\theta_0}^{\pi} \frac{\cos\theta_2}{\sqrt{2N\,(\cos\theta_2 - \cos\theta_0)}}\, d\theta_2 = 0. \tag{47c}$$

4.3 Triple point

The intersection of the two separatrix curves given by the system of equations (44) and (47), respectively, defines a triple point that can be found requiring that, in equations (47), $\theta_0 \to \pi_-$:

$$s_0 = \int_0^{\pi} \frac{1}{\sqrt{\kappa^2 + 2N\,(\cos\theta_1 + 1)}}\, d\theta_1, \tag{48a}$$

$$1 - s_0 = \lim_{\theta_0 \to \pi_-} \int_{\theta_0}^{\pi} \frac{1}{\sqrt{2N\,(\cos\theta_2 - \cos\theta_0)}}\, d\theta_2, \tag{48b}$$

$$\int_0^{\pi} \frac{\cos\theta_1}{\sqrt{\kappa^2 + 2N\,(\cos\theta_1 + 1)}}\, d\theta + \lim_{\theta_0 \to \pi_-} \int_{\theta_0}^{\pi} \frac{\cos\theta_2}{\sqrt{2N\,(\cos\theta_2 - \cos\theta_0)}}\, d\theta_2 = 0. \tag{48c}$$

The two limits in (48b) and (48c) involve the integration of a singular function in a vanishing domain and take a finite value. In Appendix A, they are calculated as

$$\lim_{\theta_0\to\pi_-}\int_{\theta_0}^{\pi}\frac{1}{\sqrt{2N\,(\cos\theta-\cos\theta_0)}}\,d\theta=\frac{\pi}{\sqrt{-4N}},\tag{49}$$

$$\lim_{\theta_0\to\pi_-}\int_{\theta_0}^{\pi}\frac{\cos\theta}{\sqrt{2N\,(\cos\theta-\cos\theta_0)}}\,d\theta=-\frac{\pi}{\sqrt{-4N}}.\tag{50}$$

Hence, (48b) provides the value of the reaction force at the triple point:

$$N=-\left(\frac{\pi}{2(1-s_0)}\right)^2,\tag{51}$$

while the two remaining equations, namely (48a) and (48c), can be rewritten as

$$s_0=\int_0^{\pi}\frac{1}{\sqrt{\kappa^2-\frac{\pi^2(\cos\theta+1)}{2(1-s_0)^2}}}\,d\theta,\tag{52a}$$

$$1-s_0=\int_0^{\pi}\frac{\cos\theta}{\sqrt{\kappa^2-\frac{\pi^2(\cos\theta+1)}{2(1-s_0)^2}}}\,d\theta.\tag{52b}$$

These equations can be solved numerically to give the values of s_0 and κ at the triple point:

$$s_0\approx 0.692,\qquad \kappa\approx 10.27.\tag{53}$$

Remark 5 All the regular elliptic integrals illustrated in this section could be formally solved in terms of elliptic functions, so that the integroalgebraic equations would read as algebraic equations only. We prefer to avoid the formalism of elliptic functions and make the paper, in our opinion, more readable. Conversely, elliptic functions are useful for a stable and accurate numerical integration and will be purposely exploited in Sect. 6.

5 Linearization

We linearize the system of equations (17) by a regular expansion around the homogeneous solution $\theta=\pi s$, $N=0$ corresponding to $\kappa=0$. A first-order perturbation in κ reads

$$\theta_1=\pi s+\varepsilon\theta_1^1(s),\qquad \theta_2=\pi s+\varepsilon\theta_2^1(s),\qquad N=\varepsilon N^1,\tag{54}$$

where ε is a smallness parameter. Substituting the approximate representation of the solution in equations (17) and collecting terms of the same order, we find

$$(\theta_1^1)''=-N_1\sin(\pi s),\qquad (\theta_2^1)''=-N_1\sin(\pi s),\qquad N_1'=0,\tag{55}$$

that can be immediately integrated to give

$$\begin{aligned}\theta_1^1(s) &= \frac{N_1}{\pi^2}\sin(\pi s) + As + B,\\ \theta_2^1(s) &= \frac{N_1}{\pi^2}\sin(\pi s) + Cs + D.\end{aligned} \tag{56}$$

The integration constants can be determined applying the boundary conditions (20) so that

$$\begin{aligned}\theta_1(s) &= \pi s + \frac{N}{\pi^2}\sin(\pi s) + \kappa(1-s_0)s,\\ \theta_2(s) &= \pi s + \frac{N}{\pi^2}\sin(\pi s) + \kappa s_0(1-s),\end{aligned} \tag{57}$$

where the small parameter ε has been reabsorbed into the definitions of N and κ. To obtain the value of the reaction N, we integrate the first component of the equation (18) enforcing the boundary and interface conditions (19). After some calculations, to first order in the perturbation, we get

$$N = -2\kappa\sin(\pi s_0), \tag{58}$$

and therefore

$$\theta_1(s) = \pi s - \frac{2\kappa}{\pi^2}\sin(\pi s_0)\sin(\pi s) + \kappa(1-s_0)s, \tag{59}$$

$$\theta_2(s) = \pi s - \frac{2\kappa}{\pi^2}\sin(\pi s_0)\sin(\pi s) + \kappa s_0(1-s). \tag{60}$$

In particular, the linearized tension (58) is always negative, regardless of the jump in curvature.

We are now able to devise the condition that, to first order, characterizes the different regimes discussed above; from a geometrical point of view, we can plot the curve that separates the regimes in the (κ, s_0) plane.

- The *quasi-ring* solution illustrated above occurs for $\theta_1(s_0) < \pi$ and small κ. It stops existing when the curve γ_1 has endpoint in $\theta_1(s_0) = \pi$, so that γ_2 collapses into a point of the phase plane. This condition reads

$$\theta_1(s_0) = \pi s_0 - \frac{2\kappa}{\pi^2}\sin^2(\pi s_0) + \kappa(1-s_0)s_0 = \pi. \tag{61}$$

- The *saddle* and the *dumbbell* solutions show up when the jump in s_0 is larger than κ, so that the curve γ_2 has left endpoint with negative curvature. The curve in the parameter plane is therefore defined by the condition

$$\theta_2'(s_0) = \pi - \frac{2\kappa}{\pi}\sin(\pi s_0)\cos(\pi s_0) - \kappa s_0 = 0. \tag{62}$$

  The points in the (κ, s_0) plane with $\theta_0 < \pi$ are pear-type solutions, those with $\theta_0 > \pi$ are saddle-like solutions.

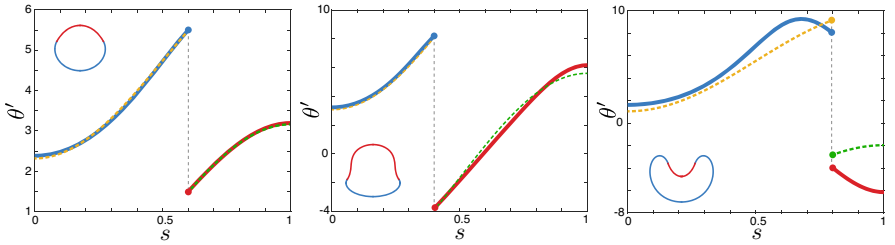

Fig. 7 Plot of the curvature of the rod with $k = 4$ and $s_0 = 0.6$ (ring, left), $k = 12$ and $s_0 = 0.4$ (dumbbell, center), $k = 12$ and $s_0 = 0.8$ (saddle, right). The jump in curvature occurs in s_0 the natural curvature of the rod has a discontinuity. In all cases, the curvature $\theta'(s)$ increases monotonically out of the jump in $s = s_0$. Light blue and red denote the nonlinear solution, whereas dashed yellow and green curves are the linear solution; they are practically superposed to the numerical solution of the fully nonlinear problem for small k and s_0 (ring)

6 Results

The solution of the nonlinear balance equations (17)–(18) with boundary conditions (19)–(20) is obtained using the Matlab function `bvp4c`. We only mention a technical detail in this respect: As the input has to be a monolithic system of first-order differential equations defined in the same domain, we mapped the domains $[0, s_0]$ and $[s_0, \ell]$ back into $[0, 1]$, we solved the equations, and then we have pushed forward the solution to plot the results. A comparison between the numerical solutions of the nonlinear problem and the analytical solution of the linear problem, as reported in Eqs. (59) and (60), is shown in Fig. 7.

When multiple solutions exist, see Fig. 3, it is natural to ask which solution is selected by the numerical algorithm used to solve the boundary value problem. Although no rigorous justification is available at this stage, our heuristic observations suggest that, after discarding self-intersecting solutions, the algorithm converges to the physically admissible solution of minimum elastic energy.

The phase diagram reported in Fig. 8 is obtained by numerical integration of equations (44) and (47). Integrals are solved in terms of elliptic functions, thus ensuring a stable and accurate numerical integration.

A careful consideration of the plot in Fig. 8 reveals that the quasi-ring solution characterizes the regime of small jump in natural curvature κ. For values of $\kappa < \pi$, the quasi-ring is the only admissible solution. This solution also persists for large κ, provided that s_0 is sufficiently small.

If the high natural curvature is concentrated in a short portion of the rod (large s_0), the saddle shape emerges. For intermediate values of s_0 and large enough κ, the rod takes the pear-like shape. There appears to be an optimal value of $s_0 \approx 0.35$ that allows the pear-shaped configuration to form at the minimum curvature jump ($\kappa \approx 5.3$). The transitions exhibit a characteristic re-entrant phase. For example, following the solutions at a fixed value of $\kappa \approx 7$ while increasing s_0 from 0, the observed morphology follows the sequence: quasi-ring, then pear-shaped, back to quasi-ring, and finally saddle-shaped.

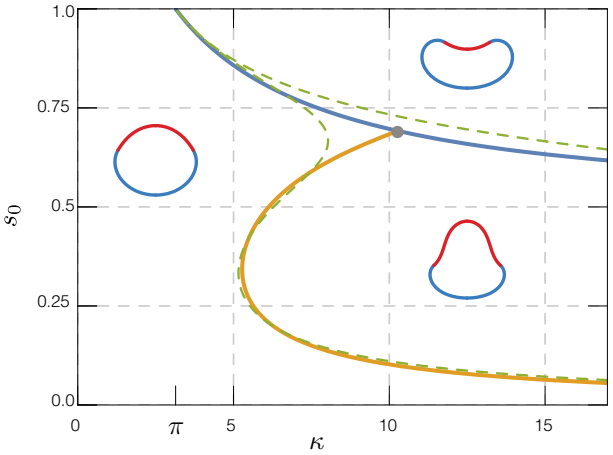

Fig. 8 Phase diagram: the plotted curves are obtained by numerical approximation of the curves defined by the integroalgebraic equations (44)–(47), corresponding to the blue and orange lines, respectively. The linearized equations yield the curves defined by equations (61) and (62), corresponding to the dashed lines

The reported diagram is universal in the sense that it dictates the morphology of every inextensible piecewise homogeneous rod, the physical length and the bending stiffness being incorporated in the non-dimensional parameters s_0 and κ. The triple point, located at $\kappa \approx 10.27, s_0 \approx 0.692$, holds special significance: It represents a limit configuration that, in principle, could be steered into a specific regime with minimum control of the parameters.

The linear theory captures the separatrix curves quite well over a large part of the phase space, a result that is somehow beyond expectations for large κ. However, linear theory fails to capture the correct morphology around the triple point, where nonlinearity plays a major role. It is not surprising that the direct numerical approximation of the Euler–Lagrange equations also fails to converge in this same region. This inherent numerical difficulty in approximating the Euler–Lagrange equations around the triple point is revealed by equation (48b): It involves integration of a singular function on a null measure set.

Final Remarks

The Euler Elastica is the classical–mechanical model to represent the mechanics of a slender planar inextensible rod. Its conceptual simplicity (no strain moduli, no transverse thickness) makes it possible to obtain universal results from its analysis, because the material parameters involved (bending stiffness, natural curvature, lengths) resume in two non-dimensional numbers. In this work, we have characterized all the possible simple shapes that can be achieved by a slender inextensible rod because of its piecewise natural curvature as a function of the jump in natural curvature and its location. Our results, and in particular the phase diagram in Fig. 8, are universal: they apply to any slender inextensible rod and they can likely provide a starting point also for the

characterization of the regimes of extensible and shearable rods of finite thickness. The generality of our results can be further appreciated by observing that equation (12b) can be understood as the application of a pointwise bending moment on a rod with homogeneous properties.

In this paper, we have considered only planar and flip-symmetric configurations. The former assumption is inherited from the physical system that has inspired this investigation, namely the cross-section of a tubular epithelial duct (Messal et al. 2019; Ambrosi et al. 2026), so that out-of-plane displacements are excluded by the geometry itself; the latter is imposed for simplicity. We only mention that non-planar equilibria can also be produced when the axis of the natural curvature is not aligned with that of the ring (Michell 1890; Goriely 2006).

Finally, we have characterized the equilibrium configurations and selected, among them, that of minimal energy. This is a mere classification and does not imply the local stability of the solution, since we only retain simple solutions. A rigorous argument for the local stability of the coexisting higher-energy branches (Kumar and Healey 2010; Jin and Bao, 2008) requires that the study of the second variation of the energy under the closure constraints (equivalently, of the Jacobi accessory equation in the presence of isoperimetric constraints) will be addressed in a future work.

Acknowledgements The authors acknowledge the financial support of the GNFM of the Istituto Nazionale di Alta Matematica (INdAM). GT acknowledges support from the Italian Ministry of University and Research through project PRIN 2022NNTZNM DISCOVER, and the "Departments of Excellence" initiative. GT also acknowledges support from the Consiglio Nazionale delle Ricerche through project "MESOFLU – Metodi Mesoscopici per i Fluidi Complessi". DA acknowledges Luca Lussardi and Marco Morandotti for fruitful discussions.

Author Contributions All authors contributed equally to the conception, development, analysis, and writing of this work.

Funding Open access funding provided by Politecnico di Milano within the CRUI-CARE Agreement.

Data Availability No datasets were generated or analyzed during the current study.

Declarations

Competing interests The authors declare no competing interests.

Open Access This article is licensed under a Creative Commons Attribution 4.0 International License, which permits use, sharing, adaptation, distribution and reproduction in any medium or format, as long as you give appropriate credit to the original author(s) and the source, provide a link to the Creative Commons licence, and indicate if changes were made. The images or other third party material in this article are included in the article's Creative Commons licence, unless indicated otherwise in a credit line to the material. If material is not included in the article's Creative Commons licence and your intended use is not permitted by statutory regulation or exceeds the permitted use, you will need to obtain permission directly from the copyright holder. To view a copy of this licence, visit http://creativecommons.org/licenses/by/4.0/.

A Calculation of the Limits (49) and (50)

Equation (48b) rewrites

$$\sqrt{2N}(1-s_0) = \lim_{\theta_0 \to \pi_-} \int_{\theta_0}^{\pi} \frac{1}{\sqrt{\cos\theta - \cos\theta_0}}\, d\theta. \tag{63}$$

Introducing the new variable $t = (\pi - \theta)/(\pi - \theta_0)$, the integral rewrites

$$\begin{aligned}\sqrt{2N}(1-s_0) &= \lim_{\theta_0 \to \pi_-} \int_1^0 \frac{\pi - \theta_0}{\sqrt{\cos(\pi + t(\theta_0 - \pi)) - \cos\theta_0}}\,(-dt) \\ &= \int_0^1 \lim_{\theta_0 \to \pi_-} \frac{\pi - \theta_0}{\sqrt{-\cos(t(\theta_0 - \pi)) - \cos\theta_0}}\, dt.\end{aligned} \tag{64}$$

Another change of variable is useful: $y = \pi - \theta_0$ so that

$$\begin{aligned}\sqrt{2N}(1-s_0) &= \int_0^1 \lim_{y \to 0^+} \frac{y}{\sqrt{\cos(y) - \cos(ty)}}\, dt = \int_0^1 \lim_{y \to 0^+} \frac{y}{\sqrt{1 - \frac{y^2}{2} - (1 - \frac{(ty)^2}{2})}}\, dt \\ &= \int_0^1 \frac{\sqrt{2}}{\sqrt{t^2 - 1}} dt = \sqrt{2} i \frac{\pi}{2}.\end{aligned} \tag{65}$$

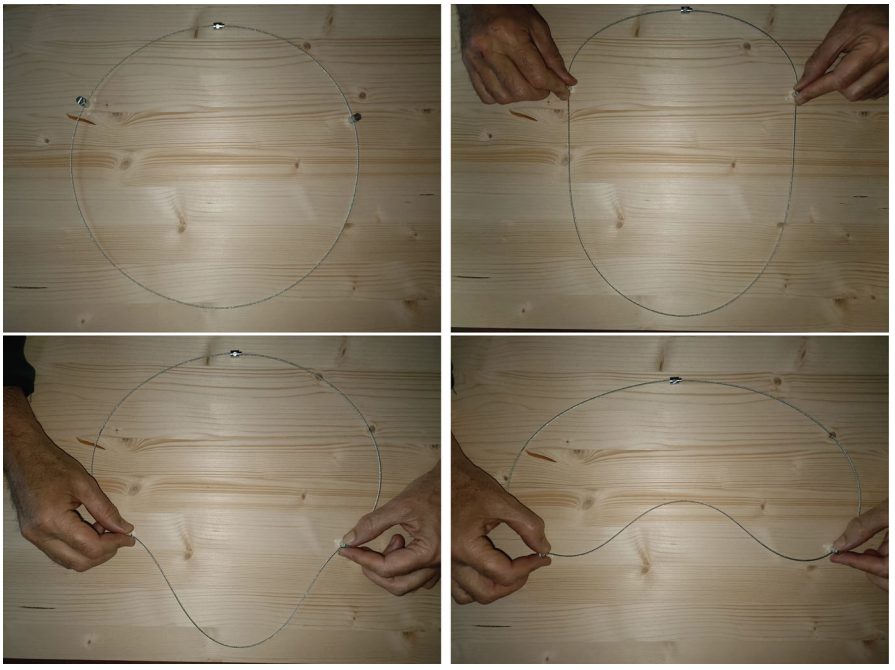

Fig. 9 Experimental illustration of the three morphological shapes: circular (top left), quasi-ring (top right), dumbbell (bottom left), and saddle (bottom right)

Analogous calculations apply to the second term at the right-hand side of equation (48c).

B A Home-made Experiment

The shapes observed in our numerical experiment can be reproduced observing that the discontinuity in curvature κ is mathematically identical to applying a pointwise bending moment. In Fig. 9 are reported the pictures of a ring of galvanized steel cable on which are applied symmetric hand-made pointwise bending moments in different curvilinear coordinates. The shapes are the ones illustrated above. The experiment is, however, very qualitative for two reasons: no measure of the exerted bending moment is known and the spatial positions of the application point is at some extent fixed.

C Bifurcation Diagram

For a fixed value of s_0, we seek for the values of κ, M, and N at which the number of equilibrium solutions changes. As described in Sect. 2, equilibrium solutions are obtained searching for the intersections of the zero-level sets of two functions in the (M, N) plane. More precisely, for fixed s_0 we define

$$F(\kappa, M, N) := \theta_2(1; \kappa, M, N) - \pi, \tag{66}$$

$$G(\kappa, M, N) := x_2(1; \kappa, M, N), \tag{67}$$

so that the simultaneous conditions

$$F(\kappa, M, N) = 0, \qquad G(\kappa, M, N) = 0$$

characterize the equilibrium configurations (see Fig. 2).

To determine where the number of solutions changes, we look for values of κ for which the two zero-level curves become tangent. This condition is detected by introducing the quantity

$$J(\kappa, M, N) = \frac{\partial F}{\partial M}\frac{\partial G}{\partial N} - \frac{\partial F}{\partial N}\frac{\partial G}{\partial M}, \tag{68}$$

which is the Jacobian determinant of the map $(M, N) \mapsto (F, G)$. Vanishing of J identifies the loss of transversality of the intersection between the curves $F = 0$ and $G = 0$. Therefore, the critical values separating regions with different numbers of equilibria are the solutions of

$$F(\kappa, M, N) = 0, \qquad G(\kappa, M, N) = 0, \qquad J(\kappa, M, N) = 0.$$

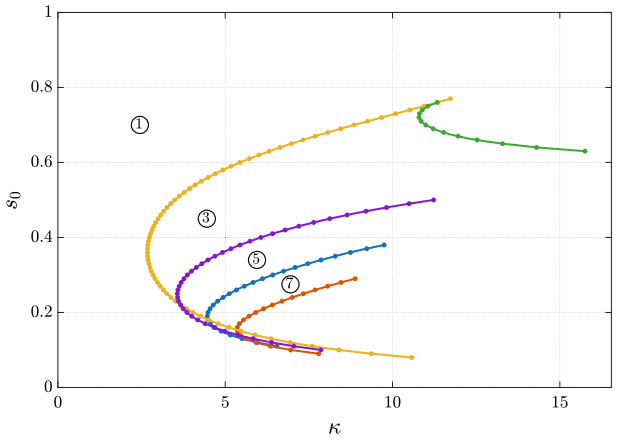

Fig. 10 Critical curves in the (κ, s_0) plane separating regions with different numbers of equilibrium solutions. The curves are obtained by solving $F(\kappa, M, N) = 0$, $G(\kappa, M, N) = 0$, and $J(\kappa, M, N) = 0$, where J is the Jacobian determinant of (F, G) with respect to (M, N). These conditions identify non-transverse intersections of the zero-level sets of F and G. For small s_0, several branches accumulate, indicating the presence of multiple mathematical solutions; for intermediate s_0, the structure reduces to a single boundary, and for $s_0 \gtrsim 0.77$ the equilibrium is unique. The insets indicate the number of equilibrium solutions (irrespective of physical admissibility) present in the corresponding region

From a numerical viewpoint, the computation proceeds in two stages. In the first stage, a coarse sweep is carried out over the ranges

$$M \in [0, 15], \qquad N \in [-500, 0], \qquad \kappa \in [3, 20].$$

Cells in which the functions exhibit a sign change are then selected as candidates for the presence of a root. In a second stage, the search is refined locally within those cells, yielding a highly accurate approximation of the critical set.

The resulting diagram is shown in Fig. 10; it identifies the loci in parameter space where the number of equilibrium solutions changes.

For small values of s_0, one observes a pronounced accumulation of critical curves, indicating the onset of regions in which multiple mathematical solutions coexist. This result does not contradict the region of uniqueness reported in Fig. 3 because the present diagram does not distinguish between physically admissible and non-admissible equilibria. Among the several solutions detected for small s_0, only one of them does not exhibit self-intersections, whereas the others correspond to self-intersecting configurations and are therefore not physically relevant.

For intermediate values of s_0, the structure becomes considerably simpler, and only one boundary curve occurs, marking a change in the number of solutions. This behavior persists up to approximately $s_0 \approx 0.77$, beyond which the solution is unique.

We emphasize that the analysis of this appendix only refers to the mathematical solution set: no additional requirement of physical admissibility (non-self-intersection) applies.

References

Ambrosi, D., Favata, A., Paroni, R., Tomassetti, G.: Oncogenic transformation of tubular epithelial ducts: How mechanics affects morphology. European Journal of Mechanics - A/Solids, 117: 105984, (2026). ISSN 0997-7538. https://doi.org/10.1016/j.euromechsol.2025.105984

Antman, S.S.: Nonlinear Problems of Elasticity. Springer-Verlag, New York (2005)

Audoly, B., Pomeau, Y.: Elasticity and Geometry: From Hair Curls to the Nonlinear Response of Shells, Oxford University Press (2010)

De Pascalis, R., Napoli, G., Turzi, S.S.: Growth-induced blisters in a circular tube. Physica D **283**, 1–9 (2014)

Favata, A., Paroni, R., Recrosi, F., Tomassetti, G.: Competition between Epithelial Tissue Elasticity and Surface Tension in Cancer Morphogenesis. Int. J. Eng. Sci. **176**, 103677 (June2022). https://doi.org/10.1016/j.ijengsci.2022.103677

Giomi, L.: Softly constrained films. Soft Matter **9**, 8121–8139 (2013)

Goriely, A.: Twisted elastic rings and the rediscoveries of Michell's instability. J. Elast. **84**(3), 281–299 (2006). https://doi.org/10.1007/s10659-006-9055-3

Goriely, A., Tabor, M.: Spontaneous helix hand reversal and tendril perversion in climbing plants. Phys. Rev. Lett. **80**(7), 1564–1567 (1998). https://doi.org/10.1103/PhysRevLett.80.1564

Haas, P.A., Goldstein, R.E.: Nonlinear and nonlocal elasticity in coarse-grained differential-tension models of epithelia. Phys. Rev. E **99**, 022411 (2019). https://doi.org/10.1103/PhysRevE.99.022411

Healey, T.J.: Global bifurcations and continuation in the presence of symmetry with an application to solid mechanics. SIAM J. Math. Anal. **19**(4), 824–840 (1988). https://doi.org/10.1137/0519057

Healey, T.J.: Stability and bifurcation of rotating nonlinearly elastic loops. Q. Appl. Math. **48**(4), 679–698 (1990)

Jin, M., Bao, Z.B.: Sufficient conditions for stability of Euler elasticas. Mech. Res. Commun. **35**, 193–200 (2008). https://doi.org/10.1016/j.mechrescom.2007.09.001

Khalilgharibi, N., Recho, P., Suzanne, M., Kabla, A., Charras, G.: Curling of epithelial monolayers reveals coupling between active bending and tissue tension. In: Proceedings of the National Academy of Sciences, (2020)

Krajnc, M., Štorgel, N., Hočevar Brezavšček, A., Ziherl, P.: A tension-based model of flat and corrugated simple epithelia. Soft Matter (2013). https://doi.org/10.1039/C3SM51588E

Kumar, A., Healey, T.J.: A generalized computational approach to stability of static equilibria of nonlinearly elastic rods in the presence of constraints. Comput. Methods Appl. Mech. Engrg. **199**, 1805–1815 (2010). https://doi.org/10.1016/j.cma.2010.02.007

Lions, J.L., Kenneth, P., Magenes, E.: Non-Homogeneous Boundary Value Problems and Applications: Vol. 1. Grundlehren der mathematischen Wissenschaften. Springer Berlin Heidelberg, (2012). ISBN 9783642651618. URL https://books.google.it/books?id=R2T7CAAAQBAJ

Manfredo, P.: do Carmo. Differential Geometry of Curves and Surfaces. Prentice-Hall, Englewood Cliffs, NJ (1976)

Messal, H.A., Alt, S., Ferreira, R.M.M., et al.: Tissue curvature and apicobasal mechanical tension imbalance instruct cancer morphogenesis. Nature **566**, 126–130 (2019). https://doi.org/10.1038/s41586-019-0891-2

Michell, J.H.: On the stability of a bent and twisted wire. Messenger of Mathematics **19**, 181–184 (1890)

Napoli, G., Goriely, A.: A tale of two nested elastic rings. Proceedings of the Royal Society A: Mathematical, Physical and Engineering Sciences **473**(2204), 20170340 (2017)

Napoli, G., Goriely, A.: Elastocytosis. J. Mech. Phys. Solids **145**, 104133 (2020)

Napoli, G., Turzi, S.: Snap buckling of a confined thin elastic sheet. Proceedings of the Royal Society A: Mathematical, Physical and Engineering Sciences **471**(2183), 20150444 (2015)

Tadjbakhsh, I., Odeh, F.: Equilibrium states of elastic rings. J. Math. Anal. Appl. **18**, 59–74 (1967). https://doi.org/10.1016/0022-247X(67)90182-5

Publisher's Note Springer Nature remains neutral with regard to jurisdictional claims in published maps and institutional affiliations.

Authors and Affiliations

D. Ambrosi[1] · A. Favata[2] · R. Paroni[3] · G. Tomassetti[4,5] · S. Turzi[6]

✉ S. Turzi
stefano.turzi@polimi.it

D. Ambrosi
davide.ambrosi@polito.it

A. Favata
antonino.favata@uniroma1.it

R. Paroni
roberto.paroni@unipi.it

G. Tomassetti
giuseppe.tomassetti@uniroma3.it

1 DISMA, Politecnico di Torino, corso Duca degli Abruzzi 24, 10129 Torino, Italy

2 Department of Structural and Geotechnical Engineering, Sapienza University of Rome, Via Eudossiana 18, 00184 Rome, Italy

3 Department of Civil and Industrial Engineering, University of Pisa, Largo Lucio Lazzarino 1, 56122 Pisa, Italy

4 Department of Engineering, Roma Tre University, Via Vito Volterra 62, 00146 Rome, Italy

5 Institute for Applied Mathematics, "Mauro Picone"- CNR, Via dei Taurini 19, 00185 Roma, Italy

6 Dipartimento di Matematica, Politecnico di Milano, Piazza Leonardo da Vinci 32, 20133 Milano, Italy